Journal of Power Sources 654 (2025) 237887

Contents lists available at ScienceDirect

Journal of Power Sources

journal homepage: www.elsevier.com/locate/jpowsour

Interplay between alkaline water oxidation temperature, composition and performance of electrospun high-entropy non-equimolar (Cr,Mn,Fe,Co,Ni) oxide electrocatalysts

Claudia Triolo [a,b,1], Kaveh Moulaee [c,1], Fulvio Bellato [d], Gioele Pagot [e], Alessandro Ponti [d], Salvatore Maida [a], Nicola Pinna [f], Giovanni Neri [c], Vito Di Noto [e,b,*], Saveria Santangelo [a,b,**]

[a] Dipartimento di Ingegneria Civile, dell'Energia, dell'Ambiente e dei Materiali (DICEAM), Università "Mediterranea", Via Zehender, Loc. Feo di Vito, 89122, Reggio Calabria, Italy
[b] National Reference Center for Electrochemical Energy Storage (GISEL), Consorzio Interuniversitario Nazionale per la Scienza e Tecnologia dei Materiali (INSTM), 50121, Firenze, Italy
[c] Dipartimento di Ingegneria, Università di Messina, Contrada di Dio, Vill. Sant'Agata, 98166, Messina, Italy
[d] Laboratorio di Nanotecnologie, Istituto di Scienze e Tecnologie Chimiche "Giulio Natta" (SCITEC), Consiglio Nazionale delle Ricerche, Via Fantoli 16/15, 20138, Milano, Italy
[e] Section of Chemistry for the Technology (ChemTech), Department of Industrial Engineering, University of Padova, Via Marzolo 9, 35131, Padova (PD), Italy
[f] Department of Chemistry, IRIS Adlershof & The Center for the Science of Materials Berlin, Humboldt-Universität zu Berlin, Brook-Taylor-Str. 2, 12489, Berlin, Germany

HIGHLIGHTS

- Non-equimolar (Cr,Mn,Fe,Co,Ni) oxides as catalysts for alkaline water oxidation.
- Catalyst with doubled Cr content is the most active at any temperature (20–60 °C).
- $Cr(OH)_3$ species on the surface of the pre-catalysts mainly control the activity.
- All surface hydroxide species contribute to enhance reaction kinetics.
- The concentration of surface oxygen-vacancies is a descriptor of the process.

GRAPHICAL ABSTRACT

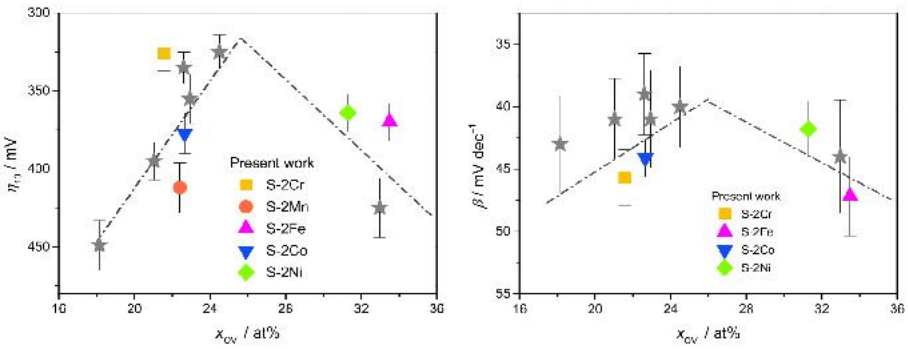

ARTICLE INFO

Keywords:
Alkaline water oxidation
High-entropy oxide
Non-equimolar (Cr,Mn,Fe,Co,Ni) oxide

ABSTRACT

High-entropy transition-metal oxides are a promising alternative to platinum group metal-based electrocatalysts for alkaline water oxidation. Their electrochemical performance can be improved by engineering surface defects and optimizing their composition. In this study, the composition of electrospun (Cr,Mn,Fe,Co,Ni) oxide nanofibers is varied by doubling the amount of each metal in turn. To obtain ultra-small (<10 nm) oxide grains with

* Corresponding author. Section of Chemistry for the Technology (ChemTech), Department of Industrial Engineering, University of Padova, Via Marzolo 9, 35131, Padova (PD), Italy.
** Corresponding author. Dipartimento di Ingegneria Civile, dell'Energia, dell'Ambiente e dei Materiali (DICEAM), Università "Mediterranea", Via Zehender, Loc. Feo di Vito, 89122, Reggio Calabria, Italy.
E-mail addresses: vito.dinoto@unipd.it (V. Di Noto), saveria.santangelo@unirc.it (S. Santangelo).
[1] C.T., and K.M. contributed equally to this work.

https://doi.org/10.1016/j.jpowsour.2025.237887
Received 17 April 2025; Received in revised form 30 June 2025; Accepted 10 July 2025

electrocatalysts
Reaction temperature
Pre-catalyst surface species

high density of surface defects, calcination is carried at low temperature (400 °C). The evaluation of nanofibers as electrocatalysts for alkaline water oxidation at different temperatures (20–60 °C) evidences that the (Cr,Mn,Fe,Co,Ni) oxide with doubled Cr concentration exhibits the highest activity at any reaction temperature (overpotentials at 10 mA cm^{-2}: 326 and 255 mV at 20 and 60 °C, respectively). The results obtained clearly prove the key role of surface defects. The oxygen-vacancy concentration is confirmed as a descriptor of the alkaline water oxidation process able to fully explain the behavior of the present electrocatalysts. The activity and the energy barrier under applied overpotential (11–33 kJ mol^{-1}) are mainly influenced by the concentration of chromium hydroxide species on the catalyst precursor surface, while all surface hydroxide species contribute to enhance reaction kinetics and control the energy barrier at equilibrium (86–147 kJ mol^{-1}).

1. Introduction

It is nowadays recognized that climate change is mainly caused by anthropogenic activities. Hydrogen is considered a clean and sustainable energy carrier, alternative to fossil fuels, which can play a key role in reducing emissions of heat-trapping greenhouse gases (GHGs), responsible for global warming. Hydrogen is produced by a variety of methods with different environmental impacts. The environmental impact of H_2 production is ranked in a color scale. "Brown/black" hydrogen is extracted from coal through gasification, while "grey" hydrogen is obtained by steam reforming of methane (the primary production method today), which releases carbon dioxide as a byproduct. If CO_2 undergoes geological capture and storage or is repurposed, the color of hydrogen produced from fossil fuels changes to "blue". "Turquoise" hydrogen is produced by thermal splitting of CH_4 with production of solid carbon, while "pink", "yellow" and "green" hydrogen is obtained by electrochemical splitting of water powered by nuclear plant, grid electricity from various sources and electricity exclusively from renewable sources, respectively. Unfortunately, the cheapest production methods are the most polluting ones, while those with lower environmental impact still have production costs that are too high, which limits their broad market penetration [1].

"Green" H_2, the only with zero CO_2 emission, could help reach the goal of zero net emissions by 2050 through the decarbonisation of transport and heavy industries and, more generally, of human activities involving high GHG emissions. Currently, water electrolysis (WE) is one of the least expensive technologies for its production. WE involves two half-reactions, the cathodic hydrogen evolution reaction (HER) and the anodic oxygen evolution reaction (OER). The latter, kinetically slower than the former, represents the rate-limiting step of the process and is the major source of energy loss. Developing highly-performing, low-cost catalysts for OER can improve the energy efficiency of electrolyzers, on which the cost of H_2 production via WE critically depends [1].

As OER catalysts in alkaline environment, Earth-abundant, inexpensive, chemically reactive, corrosion resistant and thermodynamically stable, spinel-type transition-metal (TM) oxides show similar or better performance than platinum-group metal (PGM) catalysts [2,3]. In particular, spinel-type oxides based on the high entropy concept (SHEOs), which take advantage from the synergy between their multiple metallic components [4–6], appear to be the most promising alternative to PGM-based electrocatalysts. Among them, those produced by electrospinning have the added value of being suitable for electrode manufacturing via inkjet printing [7], one of the most versatile additive technology for electrochemical applications [8]. The microstructure of catalysts and the electronic environment surrounding the active metal centers have a great impact on the intrinsic catalytic performance [9]. The presence of oxygen-vacancies (OVs) facilitates the formation of low-coordinated metal cations, enhances the adsorption of OH , and provides highly kinetic and conductive active centers for the OER process [10]. The electrochemical properties of electrospun SHEOs are strongly affected by the morphology of the fibers, concentration of the OVs on their surface, crystallization- and inversion-degree of the oxide and cation distribution in the lattice. These parameters are controlled by the TM combination and the calcination temperature of precursors [7,11].

Several descriptors have been proposed for oxygen electrocatalysis, such as the outer 3*d*-electron number [12] and the occupation of e_g orbitals at the octahedral sites [13], believed to affect the adsorption energies and binding strength of OER reaction intermediates. Very recently, Vezzù et al. [14] have proposed the OV concentration as a novel descriptor for the OER behavior of TM SHEOs. It is however still unknown what is the relative importance of these descriptors and whether one of them dominates electrocatalytic activity of SHEOs. In order to fill this gap, one needs to monitor the electrocatalytic activity while the descriptors are systematically varied.

The outer 3*d*-electron number of SHEOs can be tuned by varying the equimolar TM combination [11] or the TM molar fractions, whereas, as shown by Vezzù et al. [14], decreasing the calcination temperature of $(Cr_{1/5}Mn_{1/5}Fe_{1/5}Co_{1/5}Ni_{1/5})_3O_4$ NFs drives the e_g filling towards its optimal value and enhances both the octahedral occupation by the most redox-active species and the OV surface density, as needed to improve their electrochemical performance [5,7,15–23]. Very fast localized distortional mode of oxygen-deficient octahedra TMO_{6-x} are responsible for high effectiveness of the OER in nanofibers (NFs) calcined at 400 °C [14]. The role of lattice microstrain in multi-element solid solutions has been pointed out by a combined experimental and computational approach [24]. It results in a broad distribution of adsorption energies of intermediates, i.e. in a wide range of active sites that, in turn, has beneficial effects on OER activity.

This study focuses on non-equimolar (Cr,Mn,Fe,Co,Ni) electrocatalysts for alkaline water oxidation. To identify the optimal electrocatalyst composition, a set of five HEO NFs is prepared by doubling the amount of each metal in turn, as proposed by Nguyen et al. [15] in the case of lanthanum-based high entropy perovskite (Cr,Mn,Fe,Co,Ni) oxides. Calcination is carried out at low temperature (400 °C) to obtain ultra-small (<10 nm) sized HEO grains, high OV surface density and completely random cation distributions (Fig. S1a–e) [14]. This approach provides metastable and flexible structures [14] that enable deep pre-catalyst surface restructuring [25,26] and abundant defect sites and coordinately unsaturated atoms exposed at the surface for catalytic water oxidation [26,27]. In addition, it allows to systematically vary the outer 3*d*-electron number (Fig. S1f) and finely tuning the filling of the e_g orbitals of TM cations in octahedral sites.

Moreover, in order to infer fundamental information on the OER process, the dependence of activity and kinetics on the reaction temperature is investigated, studying OER electrochemically at various temperatures in the 20–60 °C range. At the best of the authors' knowledge, only a few studies on this topic are available in the literature [28–34]. The presented results show that the reaction temperature plays a crucial role in WE performance.

2. Experimental section

2.1. Synthesis of the electrospun electrocatalysts

The synthesis route of the electrocatalysts has been illustrated in detail in a previous paper [11]. The spinnable solution, based on stoichiometric (Cr,Mn,Fe,Co,Ni) combinations (Table S1), was prepared via

sol-chemistry. Electrospinning was operated via a CH-01 Electro-spinner 2.0 (Linari Engineering s.r.l.) at 25 ± 1 °C and 40–45 % relative air humidity. Calcination, carried out for 2 h at low temperature (400 °C), was followed by rapid, uncontrolled cooling down to room temperature (RT) to generate defects on the oxide surface [14,35,36]. Since HEOs are usually only thermodynamically stable at elevated temperatures, rapid cooling also ensured that the metastable phase of the material was kinetically trapped [37]. For further details see the Supporting Information (SI).

2.2. Physicochemical characterization

The morphology, microstructure, oxide phase(s), and surface composition of the HEO-electrocatalysts were investigated by transmission electron microscopy (TEM), X-ray diffraction (XRD), micro-Raman spectroscopy (MRS), and X-ray photoelectron spectroscopy (XPS) analyses.

A FEI Talos F200S scanning/transmission electron microscope (operated at 200 kV and equipped with an EDX spectrometer for elemental mapping) was utilized to carry out high-resolution transmission electron microscopy (HRTEM), high angular annular dark field-scanning transmission electron microscopy (HAADF-STEM) and selected-area electron diffraction (SAED) analyses, respectively. Detailed information on the NF inner morphology was gathered by projection analysis of STEM/energy-dispersive X-ray spectroscopy (EDX) maps. The latter consists in selecting a straight, constant-diameter region of a NF and project the map intensity along the NF axis. The r projection is then usually fitted to models appropriate for solid or hollow NFs [11]. In the present case, we introduce a more flexible model able to interpolate between a solid and a hollow structure. The intermediate structures are represented by the parameter τ, with $\tau \to 0$ representing a hollow structure and $\tau \geq 1$ representing a solid structure. The projections were obtained from oxygen STEM/EDX maps by integrating NF segments of length 220–650 nm. To gather structural information about the primary particles, the geometrical phase analysis (GPA) of HRTEM lattice fringes [38] was carried out. The geometrical phase of the HRTEM images was further processed [39] to produce the lattice rotation and Lagrange strain maps. The rotation maps were used to ascertain the single- or poly-crystalline nature of the grains. Due to extensive grain overlap in the images, it is difficult to individuate the boundaries of individual grains because. To recover more information from the HRTEM images, a new analysis mode was introduced in a previous paper [11] where all crystallites with the *same fringe period* in an image are simultaneously imaged, irrespective of the lattice orientation. These crystallites appear in the maps as colored patches with hue denoting the lattice. Thus, geometrical relationship between crystallites can be investigated and crystallite size can be estimated.

The XRD analysis was performed with a Bruker D2 diffractometer using Ni β-filtered Cu-K_α radiation source ($\lambda = 0.1541$ nm). Diffractograms were analyzed by the Rietveld method using Maud 2.992 software. The spatial homogeneity of the oxides was assessed by measuring Raman scattering from various random positions on each specimen. For this purpose, a NTEGRA—Spectra SPM NT-MDT confocal microscope coupled to a solid-state laser operating at 532 nm was used. Measurements were carried out in air at RT by using a low laser power (250 μW at the sample surface) to prevent local heating. The scattered light from the sample was collected by a 100X Mitutoyo objective (NA = 0.75), dispersed by an 1800 lines mm ^{1} grating and detected by a cooled ANDOR iDus CCD Camera. Spectra recorded from random positions on each specimen (probed surface area <0.6 μm^2) were then were averaged to infer reliable information on the entire sample.

XPS measurements were performed using an EnviroESCA spectrometer (Specs) equipped with an Al K_α X-ray source ($h\nu$ – 1486.6 eV). Analyses were conducted under vacuum conditions (approximately 10^{-6} mbar). High-resolution spectra were acquired with a pass energy of 50 eV, an integration time of 0.1 s per step, and a resolution of 0.1 eV per data point. To mitigate experimental errors caused by charge accumulation, spectra were calibrated by aligning the adventitious carbon peak to a BE of 284.8 eV [40]. Curve fitting and spectral decomposition were carried out using Keystone software (Specs) with a Shirley-type background model [41]. Quantification parameters were provided by Specs.

The oxidation state and site distribution of the metal ions was estimated as follows. Under the employed calcination conditions (400 °C), thermodynamic equilibrium is not yet attained and we assume that TM cations are distributed in the oxide lattice in a completely random manner [11]. Simple consideration of electronegativity and redox potentials, under the appropriate constraints, leads to the distributions depicted in Fig. S1a–e, where each cation is present in the 16*d* and 8*a* sublattices with 2:1 ratio, mirroring the ratio of occupied 16*d* and 8*a* sites. A detailed discussion on the procedure to estimate the cation oxidation state and site distribution can be found in the SI.

2.3. Electrochemical characterization

Electrochemical measurements were performed using a potentiostat/galvanostat workstation (AUTOLAB PGSTAT 204 instruments) and a three-electrode set-up. A platinum (www.metrohm.com), an Ag/AgCl (www.metrohm.com) and a catalyst-loaded screen-printed carbon electrode (SPCE, www.dropsens.com) acted as counter electrode, reference electrode and the working electrode, respectively. The catalysts (~0.4 mg cm^{-2}) were loaded onto the working area (4 mm in diameter) of SPCE. A 1 M KOH solution in demineralized water was used as the electrolyte. Its pH (≈13.77) was measured by a pH meter. Further details can be found elsewhere [11,14].

The measured potentials, $E_{Ag/AgCl}$, were converted into those referred to the reversible hydrogen electrode (RHE), E_{RHE}, via the Nernst equation, $E_{RHE} = E_{Ag/AgCl} + 0.0592\ pH - E^{0}_{Ag/AgCl}$ (with $E^{0}_{Ag/AgCl} = 0.198$ V); the overpotentials were calculated as $\eta = E_{RHE} - 1.23$ V.

The polarization curves were recorded in LSV mode and at a scan rate of 5 mV s ^{1}. The charge transfer resistance at the electrolyte/electrode interface was determined from the Nyquist plot recorded by conducting EIS measurements in the frequency range from 1 Hz to 100 kHz at an applied potential of 1.7 V (vs RHE). Experimentally measured $E_{Ag/AgCl}$ values were corrected for the ohmic drop corresponding to the uncompensated solution resistance (R_u), as extracted from Nyquist plots of EIS experiments. For further details see Refs. [11,14].

The electrochemically active surface area (ECSA) was calculated via the equation ECSA = C_{DL}/C_S, where C_{DL} denotes electrochemical double-layer capacitance of the catalyst and C_S (0.04 mF cm ^{2}, according to literature [7,42,43]) indicates specific capacitance. C_{DL} was estimated via cyclic voltammetry (CV) measurements in a non-faradaic region using different scan rates (5, 10, 20, 30, 40 and 60 mV s ^{1}).

3. Results and discussion

3.1. Physicochemical properties

3.1.1. Morphology

HEOs based on non-equimolar Cr, Mn, Fe, Co, and Ni combinations are prepared by electrospinning through the synthesis route illustrated in detail in a previous paper [11]. Samples are coded as S-2X, where X stands for the TM whose precursor concentration is doubled. Their morphology is studied by TEM and HRTEM. TEM images evidence the formation of micrometer-long NFs (Fig. S2) with granular structure (Fig. 1a j), as peculiar to electrospun oxides [11,35,44,45]. The fibers consist of densely packed nano-grains with broadly distributed size (Fig. 1k–o). The grains are crystalline in nature, as proven by their SAED patterns (Fig. S3a–e). On average, their size increases in the order S-2Ni < S-2Cr ≅ S-2Fe ≅ S-2Mn ≅ S-2Co.

HR-TEM images with discernible lattice fringes could, of course, be obtained only for the very tip of the NFs where grain overlap is largely reduced. In general, lattice fringes related to the {111}, {220}, and

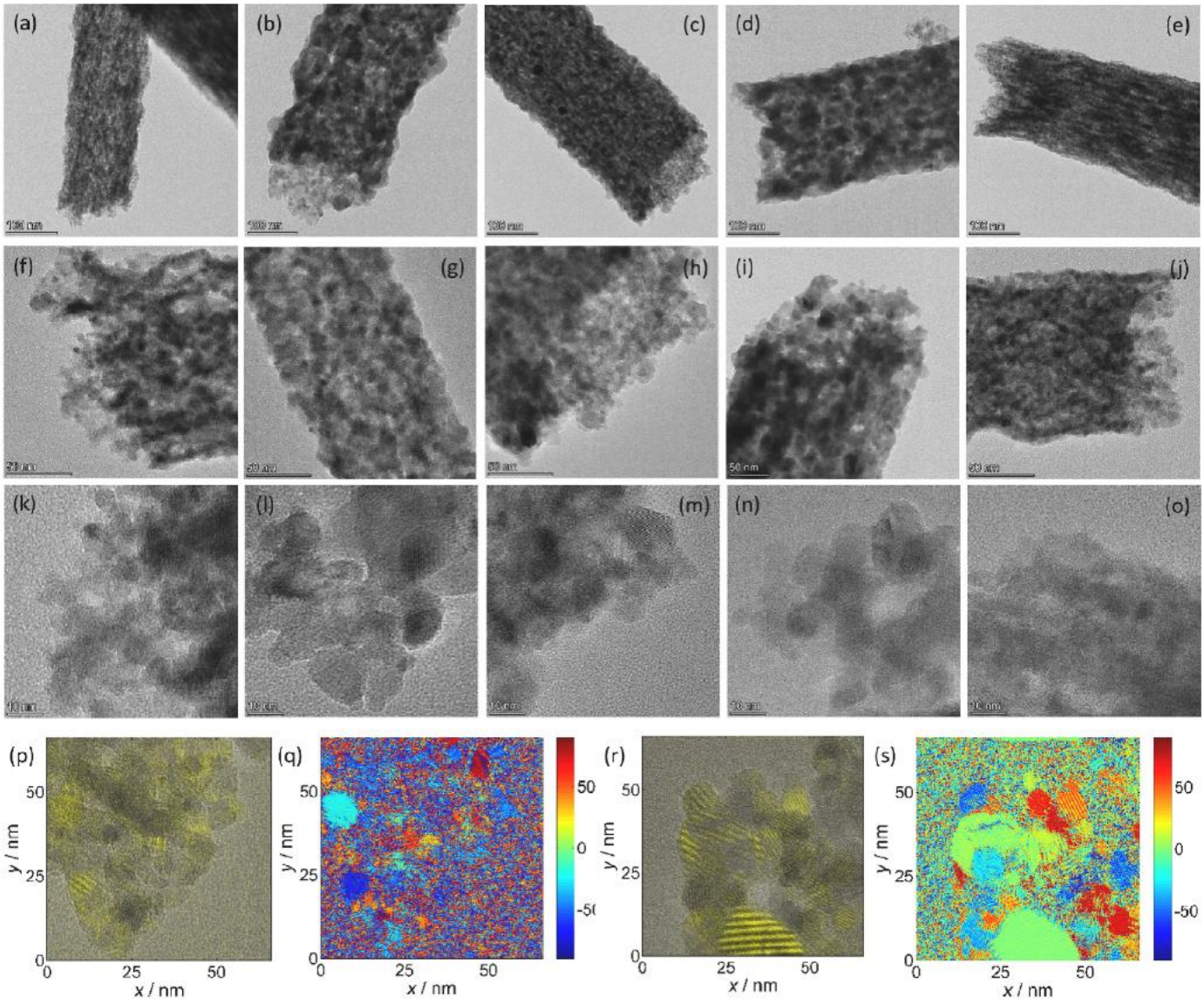

Fig. 1. (a–o) HRTEM images of electrospun NFs (a,f,k) S-2Cr, (b,g,l) S-2Mn, (c,h,m) S-2Fe, (d,i,n) S-2Co and (e,j,o) S-2Ni. (p–s) Geometrical phase analysis of HR-TEM images of a tip of S-2Cr (x,y) and S-2Mn (z,aa) NFs. Panels (p) and (r) display the HR-TEM images colorized in yellow after the intensity of the {311} fringes of the spinel lattice. Panels (q) and (s) are colorized to display the orientation of the {311} planes on the individual NCs; the color bar relates the color to the lattice orientation in degrees. (For interpretation of the references to color in this figure legend, the reader is referred to the Web version of this article.)

{311} planes of the spinel structure were detected for all NF types. However, the presence of rock-salt NCs (cfr. XRD results below), cannot be completely excluded due to the similar magnitude of the scattering vectors of the {111} and {200} planes of the rock-salt structure with those of the {311} and {400} planes of the spinel structure. HRTEM images were subjected to GPA [38,39] as in Ref. [11]. By this technique, nanocrystals (NCs) displaying lattice fringes related to the same crystal planes can be imaged individually and simultaneously (Fig. 1p–s and S4f–i). The size of the NCs at NF tips is in the range between a few and about 30 nm. The NC lattice strain, as displayed by Lagrange maps, is within a few percent of the corresponding inter-planar distance. In several cases, it could be ascertained that NCs detected by GPA coincide with individual morphological grains observed by TEM. In these cases, the very limited amount of NC internal lattice rotation shows that the grains are single crystallites. Thus, GPA results allow us to exclude a significant presence of localized defects, except maybe at the very surface of crystallites. Finally, comparing the lattice orientation of all NCs displaying a certain type of lattice fringe, in general no readily apparent geometrical relationship among the NC lattice orientation is in general observed, suggesting that the NC lattices are randomly oriented. However, in some S-2Mn and S-2Fe NF tips, many NCs display lattice fringes related to certain lattice planes, typically {311}, suggesting that a certain degree of texturing may be present.

Compositional analysis by HRTEM/EDX reveals that deviations from the nominal TM combination depend on the metal with doubled concentration (Fig. S3n–r). In S-2Ni, the metal combination is the closest to the nominal one. The molar fractions of manganese and cobalt are always higher than the nominal value; conversely, that of iron is always lower.

The uniformity of the spatial distribution of Cr, Mn, Fe, Co and Ni cations throughout the fibers at the nano-scale is investigated by STEM/EDX. The elemental maps (Fig. 2a and b and S3f–m) evidence the formation of multicomponent solid solutions in all NFs. In order to investigate the radial morphology and elemental distribution, the maps are analyzed with projection method [46]. The analyzed NFs have diameters between 100 and 400 nm. All NFs have a partially hollow

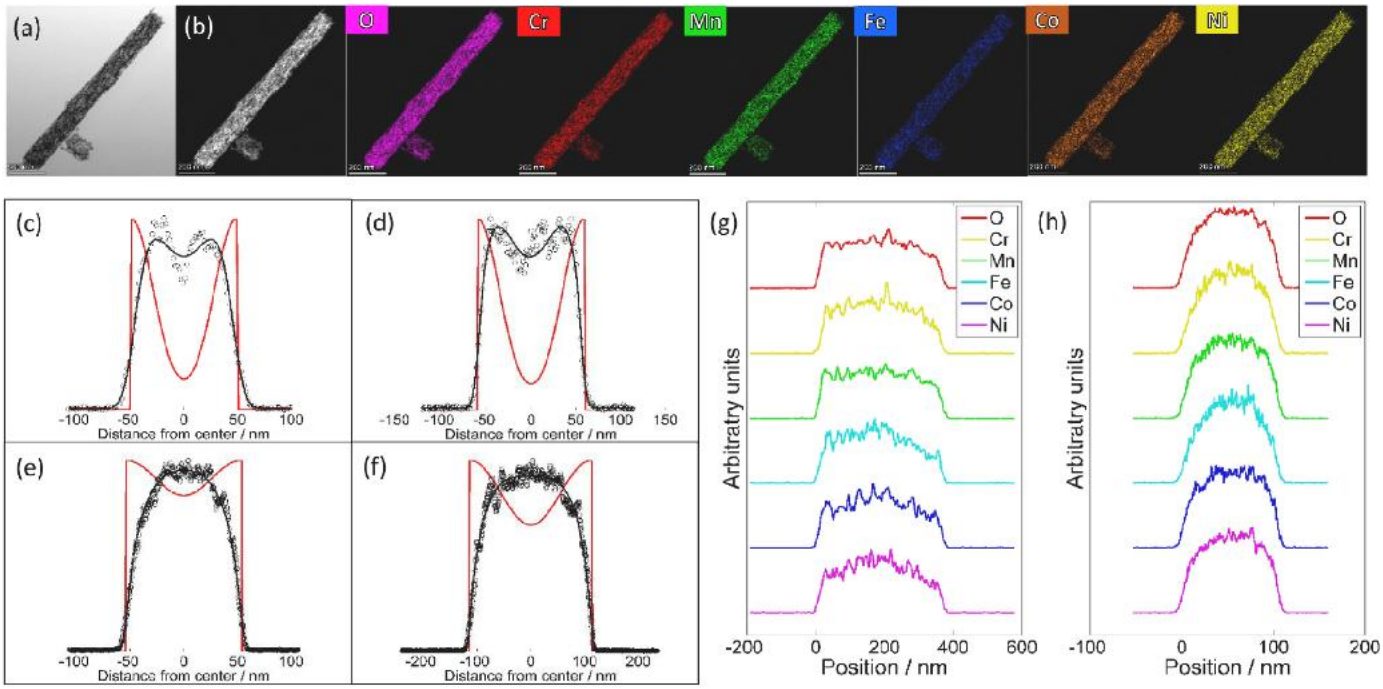

Fig. 2. (a) BF-STEM and (b) HAADF-STEM image of S-2Cr, followed by the elemental maps. (c–f) Projected profile of the oxygen elemental map of four NF. (c) S-2Cr, (d,e) S-2Fe, (f) S-2Ni. Circles: projected profile from experimental map; black line: best-fit profile; red line: radial density reconstructed from the best-fit profile. (g,h) Projected profiles of the elemental maps of two NFs. (g) S-2Mn, (h) S-2Ni. In (g) a flatter Mn profile indicates a slight concentration of Mn towards the NF surface and in (h) a more dome-like shape of the Cr and Fe profiles indicates a slight concentration of these elements towards the NF axis. (For interpretation of the references to color in this figure legend, the reader is referred to the Web version of this article.)

morphology intermediate between a solid morphology (constant radial density) and a cylindrical shell. Examples in Fig. 2c–f display the experimental projected profile, the best-fit profile and the radial distribution of oxygen in selected NFs. The shape of the oxygen profile and radial distribution vary within a NF type (Fig. 2d and e) almost as much as across the NF types (Fig. 2c–f), so the excess cation does not seem to affect the NF morphology. The metal cation projected profiles are similar, in accordance with the cation disorder of HEOs. Nonetheless, they show subtle differences, suggesting that cations may have different radial distribution. As above, such differences within a NF type vary as much as across the NF types. However, as shown in Fig. 2g,h and S4, it can be noted that (i) in all NF types, except for S-2Ni NFs, Mn tends to concentrate towards the NF surface, and (ii) in S-2Ni NFs, Cr and Fe tends to concentrate about the NF axis (center).

3.1.2. *Phase(s) and crystallization degree of the oxide*

The phase(s) of the oxide, its crystallization degree and spatial uniformity are investigated by XRD and MRS analyses. Fig. 3a displays the

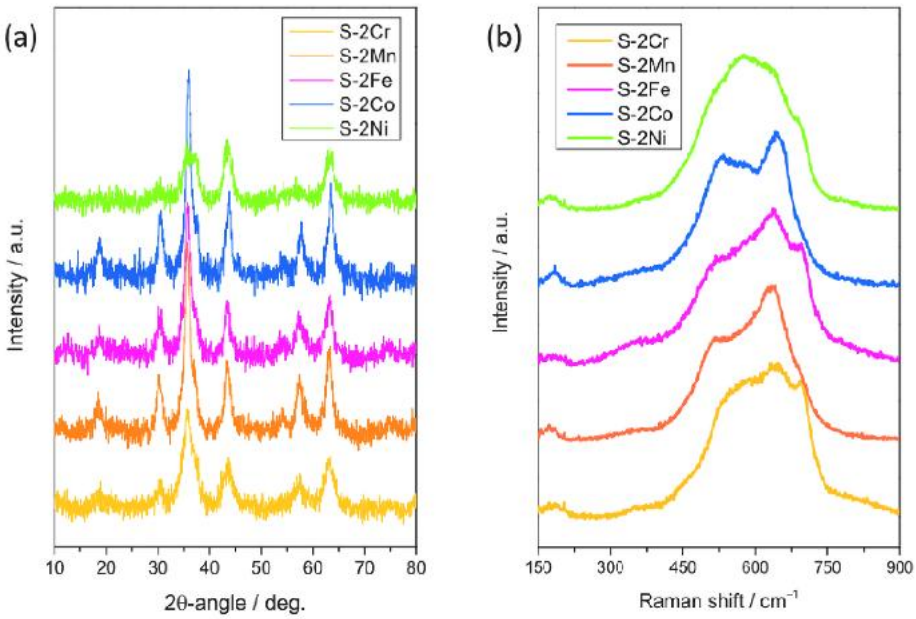

Fig. 3. (a) XRD patterns and (b) averaged micro-Raman spectra.

diffractograms recorded on the NFs. Apparently, only reflections from the (111), (220), (311), (222), (400), (422), (511) and (440) planes of the spinel structure (*Fd-3m* space group) are present in the XRD patterns, as in the case of electrospun $(Cr_{1/5}Mn_{1/5}Fe_{1/5}Co_{1/5}Ni_{1/5})_3O_4$ NFs calcined at the same temperature [14]. In order to ascertain the formation of pure single-phase spinel oxides, Rietveld refinements from XRD data are conducted (Fig. S5). The results (Table S2) reveal the formation of a secondary high-entropy oxide phase with rock-salt structure (RHEO, *Fm-3m* space group) in all NFs. Its relative amount is below 10 % in samples S-2Cr, S-2Mn and S-2Fe, about 13 % in S-2Co and reaches 30 % in S-2Ni. The average size of nano-domains with spinel structure (3.5−8.9 nm) is smaller than that of nano-domains with rock-salt structure (8.4−16 nm). The average size of HEO crystallites (d_{HEO} in Table S2), calculated as a weighted average of the sizes of nano-domains with spinel and rock-salt structure, ranges between 5.0 and 9.2 nm, in agreement with the results of the GPA of HR-TEM images. Nano-domains are generally not affected by microstrain (Table S2). Only the lattice of S-2Cr and, to a minor extent, the RHEO phase of S-2Ni show significant microstrain, which is beneficial for OER [24].

In order to evaluate the spatial homogeneity of the samples, Raman scattering is measured from several random locations on each specimen (Fig. S6). Spectra recorded in samples S-2Cr (Fig. S6a), S-2Mn (Fig. S6b), S-2Fe (Fig. S6c) and S-2Co (Fig. S6d) exhibit no significant differences in the spectral profiles, which indicates a uniform spatial distribution of the HEO nano-domains with different lattice structure. On the contrary, in sample S-2Ni (Fig. S6e), spectral profiles relative to different locations are even remarkably different, implying the lack of spatial distribution at the scale probed by MRS. In some locations, the spectra exhibit a strong similarity to the typical profile of defect-rich RHEO [47]. This finding suggests that in sample S-2Ni, nano-domains with rock-salt structure are organized in larger clusters.

Fig. 3b displays the averaged micro-Raman spectra. As in the XRD patterns, only the Raman fingerprint of the primary SHEO phase is clearly visible in the spectra. As discussed in detail elsewhere [46], the frequency positions and relative intensities of the five Raman-active vibration modes ($A_{1g} + E_g - 3F_{2g}$) of the spinel oxides are sensitive to the distribution of cations in the lattice [48] and to their radii [49]. The variation of Cr, Mn, Fe, Co, and Ni molar fractions and the consequent changes in the cation distribution (Fig. 1) mainly affects the spectral region where the $F_{2g}(2)$, $F_{2g}(3)$ and A_{1g} vibrational modes are detected (450−750 cm^{-1}). The A_{1g} peak intensifies in the NFs (S-2Mn and S-2Co) composed by slightly larger grains, as previously observed in $(Cr_{1/5}Mn_{1/5}Fe_{1/5}Co_{1/5}Ni_{1/5})_3O_4$ NFs calcined at higher temperature [11]. In the sample with the highest rock-salt component (S-2Ni), the one-phonon longitudinal optical mode (1P-LO) of the defect-rich RHEO lattice, peaking at *ca.* 550 cm^{-1}, clearly contributes to the Raman intensity (Fig. 3b). Indeed, the fitting of the spectra to Gaussian bands (Fig. S7a−e) evidences the presence of such a contribution in all spectra. Its relative intensity is linearly correlated with the relative amount of the RHEO phase, as resulting from the Rietveld refinements to the XRD data (Fig. S7f).

3.1.3. Surface composition

Since OER is inherently a surface process, understanding the surface properties of the electrocatalyst is critical to process optimization. The surface composition was investigated by XPS analysis. XPS survey spectra (Fig. S8) confirm the presence of cobalt (Co), nickel (Ni), chromium (Cr), iron (Fe), manganese (Mn), oxygen (O), and adventitious carbon (C) on the surface of the HEO electrocatalysts. The elemental composition varies across the different materials analyzed (Table S3), highlighting the selective migration of TMs to the nanoparticle surface. The surface concentration of the TM with nominally doubled molar fraction (i.e. 1/3) increases in the order Fe < Ni < Cr < Co < Mn, reaching approximately 27, 29, 31, 35, and 40 at.% respectively (Table S4 and Fig. S9). Considering TMs with nominal molar fraction 1/6, the Ni surface content is lower compared to the other metals, except in the S-2Fe sample. The surface concentrations of Co and Mn is around 20 at.% in all samples, apart from Mn in S-2Fe, where it reaches *ca.* 24 at.%. Fe and Cr surface concentrations are typically in the range of 13–15 at.%, with exceptions for Cr in S-2Ni (*ca.* 17 at.%) and Fe in S-2Co (*ca.* 21 at.%). The surface oxygen concentration sets between 70.1 and 72.5 at.%, apart from S-2Fe sample where it reaches a value of 75.4 at.%.

High-resolution XPS analyses offer detailed quantitative and qualitative insights into the oxidation states of surface elements in the HEO electrocatalysts. However, overlapping Auger lines from various TMs may introduce challenges in spectral interpretation. In the Fe $2p_{3/2}$ region (Fig. 4a), a peak at approximately 710.5 eV indicates the presence of Fe in the +3 oxidation state [50,51]. An additional feature in this region corresponds to the Co and/or Ni LMM Auger peaks. The Co $2p_{3/2}$ region (Fig. 4b) shows two peaks at approximately 780.6 and 782.2 eV, attributed to CoO and $Co(OH)_2$ species, respectively [11,52,53]. The Fe LMM Auger peak also overlaps in this region. Similarly, the Ni $2p_{3/2}$ spectrum (Fig. 4c) reveals two distinct features at approximately 854.7 and 856.1 eV, corresponding to NiO and $Ni(OH)_2$, respectively [11,54,55]. The Mn $2p_{3/2}$ spectrum (Fig. 4d) exhibits peaks at 642.0 and 645.7 eV, associated with Mn(III) and the Ni LMM Auger peak, respectively [4,11]. Finally, the Cr $2p_{3/2}$ spectrum (Fig. 4e) reveals Cr in three distinct chemical environments: (i) Cr(III) oxide (575.7 eV), (ii) Cr(III) hydroxide (576.8 eV), and (iii) Cr(VI) oxide (578.9 eV) [11,56,57]. Summarizing, Mn and Cr exhibit higher oxidation states (+3 or beyond), whereas Co and Ni predominantly appear in their +2 oxidation states.

The O 1s spectra for all samples (Fig. 5) display four distinct features: (i) a peak at approximately 529.8 eV, attributed to lattice oxygen (O_L) [58–60]; (ii) a peak near 531.1 eV, associated with surface oxygen vacancies (O_V), where surface oxygen anions adjacent to lattice vacancies are passivated with hydrogen [59,61,62]; and (iii, iv) peaks at 532.1 and 533.3 eV, corresponding to adsorbed or chemisorbed oxygen species such as O_2 or H_2O [7,46,63]. Quantitative analysis (Table S5) reveals that O_L dominates across all samples, with O_V accounting for approximately 22 at.% in most cases. However, the S-2Fe and S-2Ni samples stand out with an O_V concentration of 33.5 and 31.3 at.%, respectively. In S-2X samples, adsorbed oxygen species varies with X. Moreover, a larger adsorbed oxygen species amount is detected in those samples where a high O_V concentration is detected (*i.e.*, S-2Fe and S-2Ni samples).

3.2. Electrocatalytic performance

3.2.1. Effect of HEO composition

The OER performance of all S-2X NFs is evaluated in 1M KOH electrolyte solution, at 20 °C, using a three-electrode setup. The dependence of catalytic activity and OER kinetics on HEO composition is investigated by recording the polarization curves of all S-2X NFs in linear sweep voltammetry (LSV) mode (Fig. 6a) and by plotting their linear part (Tafel curves, Fig. 6b).

The catalytic activity, as monitored by the overpotential at 10 mA cm^{-2} (η_{10}), improves in the order S-2Mn (412 mV) < S-2Co (377 mV) < S-2Fe (370 mV) < S-2Ni (364 mV) < S-2Cr NFs (326 mV), while the kinetics, as displayed by the Tafel slope (β), fastens in the order S-2Mn (59.3 mV dec^{-1}) < S-2Fe (47.2 mV dec^{-1}) < S-2Cr (45.7 mV dec^{-1}) < S-2Co (44.1 mV dec^{-1}) < S-2Ni (41.8 mV dec^{-1}). All η_{10} and β values well compare with those reported for other spinel structured catalysts (e.g. Ni-, Ni/Co- and Co-ferrites prepared by conventional citric acid-assisted sol-gel combustion method: 381−477 mV and 46.4−73.0 mV dec^{-1}, respectively) [64] and other HEO-based catalysts (Table S6). Moreover, HEO electrocatalyst with doubled Cr concentration has lower Tafel slope than both more expensive commercial IrO_2 and RuO_2 catalysts and ranks between IrO_2 and RuO_2 with regard to overpotential at 10 mA cm^{-2} (Table S6). It exhibits almost the same activity as lanthanum-based high entropy perovskite oxide with optimized composition $La(CrMnFeCo_2Ni)O_3$ [15], but have faster kinetics (Fig. S10). Although all remaining S-2X NFs are less active than other lanthanum-based high entropy perovskite

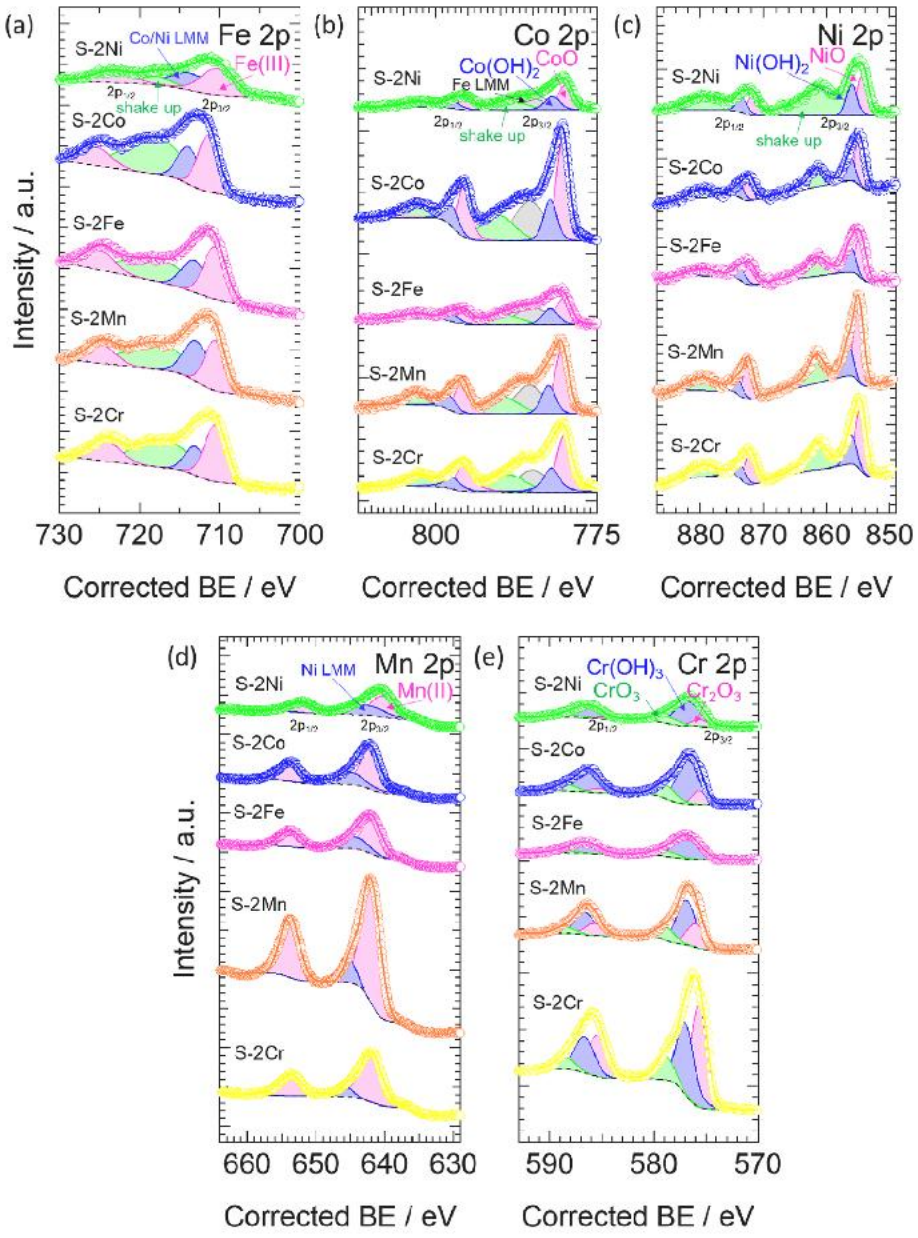

Fig. 4. High-resolution XPS curves and fitting in the analyzed spectral regions: (a) Fe 2p, (b) Co 2p, (c) Ni 2p, (d) Mn 2p, and (e) Cr 2p core levels.

oxides (P-2X), their kinetics is always faster.

3.2.2. *Role of surface defects*

No obvious relationship is observed between η_{10} and β values of S-2X electrocatalysts and the commonly adopted descriptors, i.e. outer 3*d*-electron number [12] (N_{3d}, Fig. S1f) and occupation of e_g orbitals at the octahedral sites [13] (e_g, Fig. S1g). On the contrary, when plotted against the concentration of surface OVs (x_{OV}, Table S5), which has been very recently proposed by Vezzù et al. [14] as a descriptor for the OER of spinel-type electrocatalysts, η_{10} and β values of S-2X electrocatalysts align along the volcano plots previously obtained for $(Cr_{1/5}Mn_{1/5}Fe_{1/5}Co_{1/5}Ni_{1/5})_3O_4$ NFs calcined at different temperatures (Fig. 6c and d) [14], thus confirming the generality of the proposed descriptor. The only exception is the β value of S-2Mn NFs. Being close to 60 mV dec^{-1}, it indicates that the rate-determining step (RDS) of OER process for S-2Mn NFs is represented by the formation of adsorbed *O species ($^*OH + OH^- \rightarrow {}^*O + H_2O + e^-$) [4,11], as in the case of Mn-rich $ZnMn_{2-x}Co_xO_4$ [65]. Differently, the remaining S-2X NFs exhibit lower β values showing that the RDS is the creation of O–O bonds on the material surface ($^*O + OH^- \rightarrow {}^*OOH + e^-$).

It is commonly agreed that in an alkaline solution, OER proceeds through a four-step proton-coupled electron transfer [66], involving the adsorption of four hydroxide anions at the catalyst surface with release of four electrons, two water molecules and oxygen ($4\ OH^- \rightarrow 4\ e^- + 2H_2O + O_2$, Fig. S11) [67]. Two different mechanisms are generally invoked in the literature to explain this process, namely the adsorbate evolution mechanism [9,11,14,67] (AEM, Fig. S11) and the lattice-oxygen mechanism [9,66] (LOM), which substantially differ in the nature of the active site (metal or lattice-oxygen, respectively). Here, oxygen-deficient octahedra MO_{6-x} on the catalyst surface are regarded as the active centers for the OER through the AEM mechanism [11,14,68].

To evaluate the intrinsic activity of S-2X catalysts the electrochemically active surface area (ECSA) was estimated via CV measurements. The obtained C_{DL} values (Fig. S12a, 2.5–4.7 mF) were comparable with those reported by other authors for similar nanomaterials [7,43]. Also ECSA of present S-2X electrocatalysts (62–117 cm^2) was in line with that reported in the literature for other HEOs [7,43]. The intrinsic

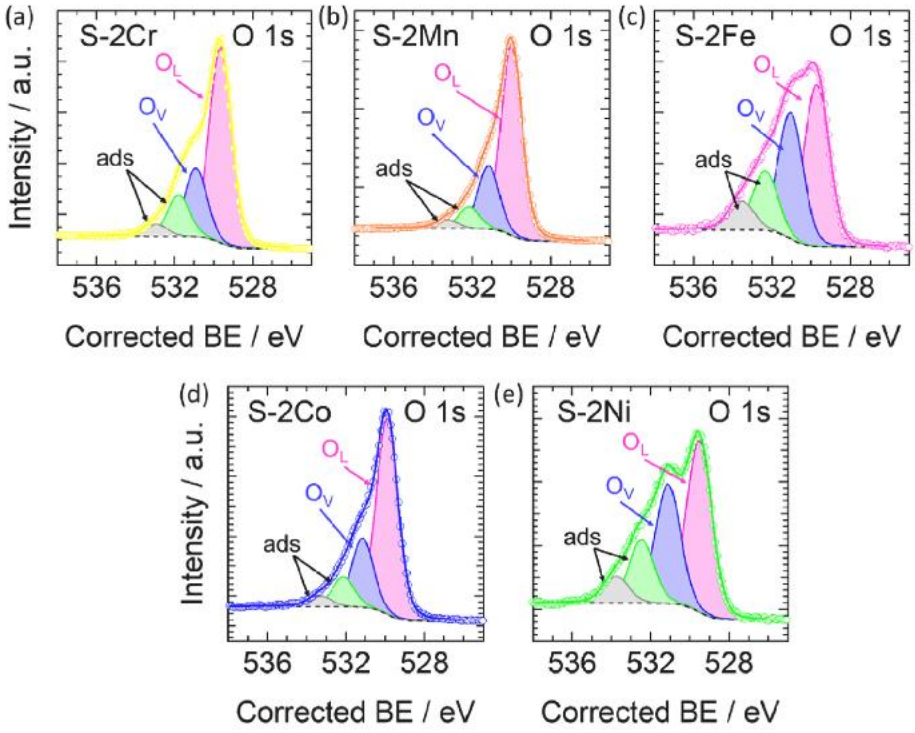

Fig. 5. High resolution XPS curves and fitting in the O 1s spectral region for (a) S-2Cr, (b) S-2Mn, (c) S-2Fe, (d) S-2Co and (e) S-2Ni samples.

activity as resulting from LSV curves normalized to the ECSA (Fig. S12b) increased in the order S-2Mn < S-2Co = S-2Ni < S-2Fe < S-2Cr, with no evident relationship with the above descriptors. Following ref. [14], the intrinsic activity was calculated also by normalizing the current density to x_{OV}, i.e. to the density of *potentially* active MO_{6-x} centers on the catalyst surface [14]. Except for sample S-2Fe, featured by the smallest ECSA value, the intrinsic activity varied in the same order as obtained by normalization to ECSA, with S-2Mn and S-2Cr exhibiting the lowest and the highest activity, respectively. The small discrepancy could be understood by plotting ECSA as a function of x_{OV} (Fig. S12d). A volcano plot is obtained, proving that the concentration of surface OVs is a reliable descriptor also for this parameter and that an optimal x_{OV} range does exist. As previously shown [14], the three-dimensional mobility of OVs is associated to structural relaxation of spinels. When $x_{OV} > 33$ %, ECSA drops, probably because the delocalization of the distortional motion of the superficial complexes inhibits their contribution to the electrocatalytic performance of the catalyst. This hypothesis might explain the discrepancy observed.

The very high activity of S-2Cr might benefit from its higher phase purity and the significant microstrain affecting its lattice (Table S2) since local strain affects activities of the stable bonding configurations [24]. According to Baek et al., [24] Cr is hugely beneficial to the activity of the Cr,Mn,Fe,Co,Ni solid solution. Indeed, in recent years, chromium is gaining increasing attention in electrocatalysis. The incorporation of Cr^{3-} into OER catalysts has been shown to substantially improve their activity and stability by adjusting the electronic structure and enhancing the electronic conductivity [69,70]. Although the empty e_g orbitals of Cr^3 favor a strong bonding to OER intermediates, its $t_{2g}^3 e_g^0$ electronic configuration considerably enhances the charge transfer and conductive nature of the catalyst. Also Cr species with higher oxidation states are beneficial to OER. Thanks to its electronic configuration ($t_{2g}^0 e_g^0$), Cr^{6+} cations can attract more electrons, thus resulting in more OH^- groups being adsorbed on the exposed Cr sites [71], stabilizing the high-valence state of active sites to exhibit superior OER activity [70], and exerting a substantial influence on lowering the adsorption free energies of the intermediates at the active sites, synergistically playing a buffer role in the multi-electron transfer process of OER [69]. Moreover, recent density functional theory (DFT) calculations demonstrate that Cr favors the transition of TM (Fe, Co, Ni) hydroxides to the active oxyhydroxide phase [72]. Further studies are underway to investigate, by means of DFT calculations, the correlations between the electronic properties governing the structural and physicochemical features of the materials and their electrochemical activity.

The surface of S-2Cr NFs is the richest in both Cr^{3+} and Cr^{6+} species (Table S3–S5). Besides, S-2Cr NFs exhibit the strongest oxidation peak and a negative shift of onset OER potential (inset of Fig. 6a), indicating an increased amount of charge transfer [73]. Oxidation peaks [11,33,74,75], detected in the low-voltage region of the j *vs* η curves of all NFs, indicate pre-catalyst surface restructuring [76] with formation of self-assembled amorphous high-entropy oxyhydroxides (HEOHs) [5,11], from oxide-/hydroxide-species reacting with water molecules under applied potential [5,17,73,77]. This process involves transition from the more stable (lower) valence states of the TM cations on the pre-catalyst surface/subsurface to their more electrocatalytically active (higher) valence states, widely recognized as the true active components in OER electrocatalysis [72,73,76,78], HEOHs, responsible for the redox centers acting as OH^- adsorption sites [75], enhance the conductivity of electrocatalyst and accelerate the charge transfer and OER process [77]. Catalyst species with ultra-small size (<10 nm, as in the present case) lead to faster rate and greater depth of reconstruction [25,73], while Cr species act as host for charge transfer from the TM neighboring cations for the generation of active high-valence species [72,78].

Actually, η_{10} is linearly correlated with the concentration of surface $Cr(OH)_3$ species (Fig. 6e), while no correlation is found with other hydroxide species (Fig. S13a–c). The higher concentration of surface $Cr(OH)_3$ species on the pre-catalyst, the more active the catalyst after activation (the lower η_{10}). As for β, it shows a better correlation with the concentration of all hydroxide species ($Cr(OH)_3$, $Co(OH)_2$ and $Ni(OH)_2$) present on the surface of the HEO fibers (Fig. 6f) than that with the concentration of surface $Cr(OH)_3$ species only (Fig. S13f). This finding proves that all surface hydroxide species synergistically cooperate in enhancing kinetics (lowering β).

To gain deeper insight into the OER process and understand the effect of electrical conductivity on the electrocatalytic performance,

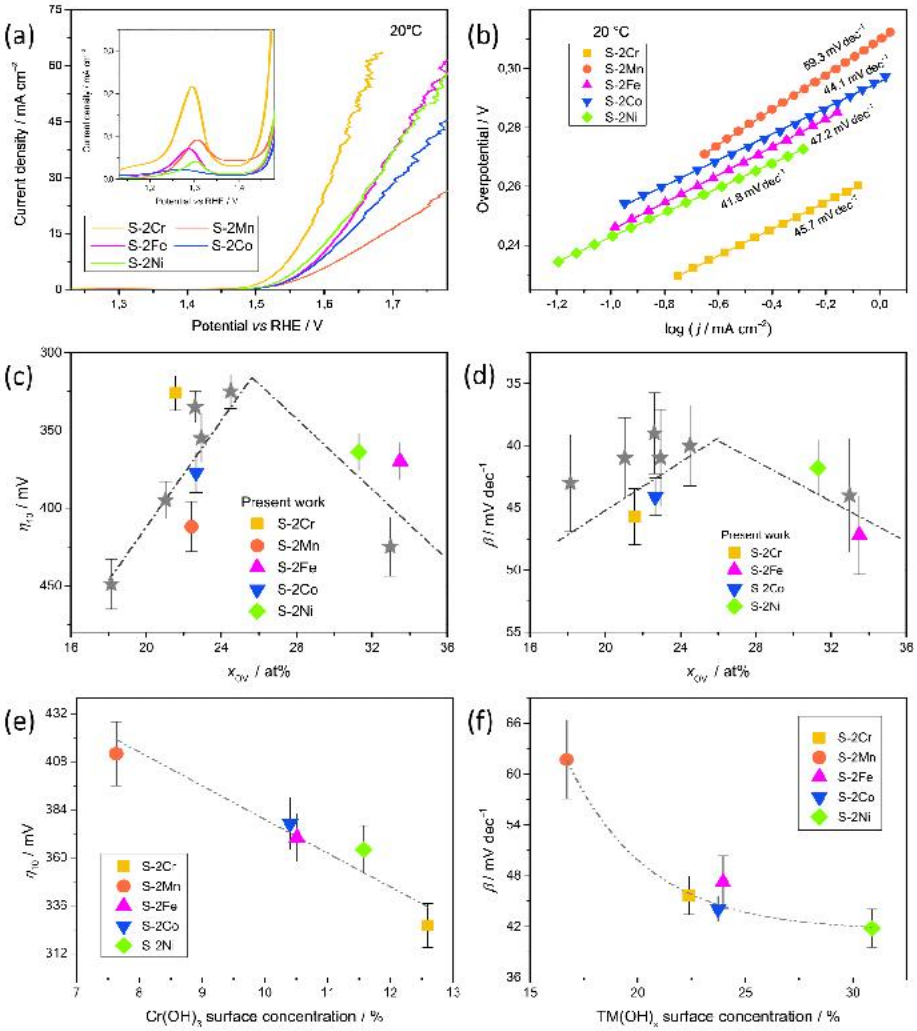

Fig. 6. (a) LSV curves in 1.0M KOH (measured pH value ≈ 13.77) at 20 °C reaction temperature (inset: pre-onset region). (b) Tafel plots for the five catalysts. (c) Overpotentials measured at 10 mA cm ^{2} (η_{10}) and (d) Tafel slopes (β) as a function of the surface OV concentration (x_{OV}). Grey stars refer to equimolar $(Cr_{1/5}Mn_{1/5}Fe_{1/5}Co_{1/5}Ni_{1/5})_3O_4$ NFs calnined under different conditions [14]. (e) η_{10} as a function of the concentration of surface Cr(OH)$_3$ species and (f) β as a function of the concentration of all surface hydroxide species.

electrochemical impedance spectroscopy (EIS) analysis is carried out and the charge transfer resistance (R_{CT}) is calculated from the resulting Nyquist plots (Fig. S14a) [26]. Interestingly, R_{CT} linearly decreases with increasing concentration of surface Cr(OH)$_3$ species (Fig. S14b), similarly to η_{10}.

3.2.3. *Effect of oxygen evolution reaction temperature*

The dependence of the catalytic activity of all S-2X NFs on reaction temperature (T_R) was investigated by recording the polarization curves at 20, 30, 40 and 60 °C (Fig. S15a–e). With increasing T_R, η_{10} decreases for all NFs (Fig. S15f), with S-2Cr always showing the best performance.

With the exception of S-2Mn NFs (featuring the smallest concentration of surface hydroxide species), with increasing T_R, the pre-onset

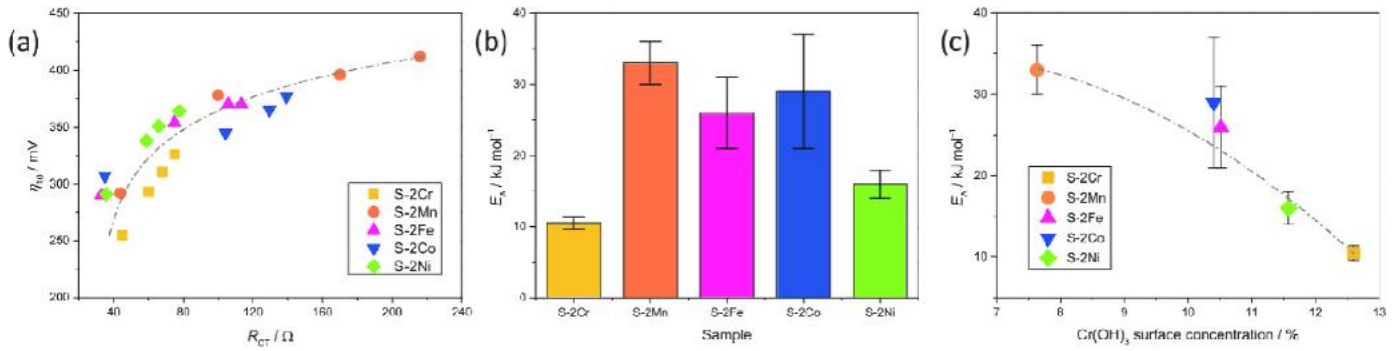

Fig. 7. (a) Increase of η_{10} with R_{CT}. (b) Activation energy (E_A), estimated as the slope of the Arrhenius plots of R_{CT}, and (c) its dependence on the concentration of surface Cr(OH)$_3$ species.

oxidation peak shifts towards lower η values (insets of Fig. S15a–e). An analogous behavior has been reported for Ni-Co oxide solid solution catalysts produced by flame pyrolysis [33]; it indicates that, at higher T_R, the surface restructuring process is favored and more active HEOH sites can be generated at a lower applied potential [33], as expected [76].

The increase of T_R promotes the decrease of R_{CT} in all electrocatalysts (Fig. S15g). Interestingly, η_{10} monotonically increases with R_{CT} (Fig. 7a). Thus, the smaller R_{CT}, the more efficient charge transfer during the OER is and the higher the catalytic activity, in agreement with previous findings on $(Cr_{1/5}Mn_{1/5}Fe_{1/5}Co_{1/5}Ni_{1/5})_3O_4$ NFs [14].

The apparent activation energy barrier (E_A) is estimated as the slope of the Arrhenius plots of R_{CT} (Fig. S15h). E_A, whose values range between 10.5 kJ mol^{-1}, in the case of S-2Cr, and 33 kJ mol^{-1}, in the case of S-2Mn (Fig. 7b), monotonically decreases with increasing concentration of surface $Cr(OH)_3$ species (Fig. 7c). This finding indicates that the presence of these species on the surface of catalyst precursors is beneficial for OER, as they favor surface restructuring and local transition to the active oxyhydroxide phase.

To study the T_R-dependence of OER kinetics, Tafel plots, $\eta = c + \beta \log_{10}(j)$, are considered (Fig. S16a–e). The Tafel slopes (Fig. S16f) indicate that the RDS of OER for each catalyst does not change with T_R. However, with increasing T_R, β increases for all NFs, with S-2Ni always showing the fastest kinetics. Thus, at higher T_R, overpotential needed to obtain a current density of 10 mA cm^{-2} lowers, but the kinetics slows down (Fig. S17a).

The Butler-Volmer equation [79] expresses the overpotential as $\eta = 2.303\, c + (2.303\, R/\alpha F)\, T \ln(j)$, where $R = 8.314$ J mol^{-1} K^{-1} and $F = 96500$C mol^{-1} are the universal gas constant and Faraday's constant, respectively, and α ($0 < \alpha < 1$) is the transfer coefficient. Except for S-2Cr, β *vs* T_R curves are nearly linear (Fig. S17b) in agreement with the Butler-Volmer equation. The α values inferred from the slopes of β *vs* T_R lines vary in the 0.49–0.64 range.

Further significant insight can come from the study of the reaction kinetics at the equilibrium ($\eta = 0$). For this purpose, the exchange current density (j_0) is determined by extrapolating the linear portions of the log(j) vs η curves at $\eta \to 0$ (Fig. S18a) [79]. Studying the T_R-dependence of j_0 allows one to estimate the activation energy (E_A^0) of the OER as the slope of the Arrhenius plots of j_0 (Fig. S18b). The results are shown in Fig. 8a. The lowest and the highest E_A values pertain to S-2Mn (86 kJ mol^{-1}) and S-2Ni (147 kJ mol^{-1}), respectively. The E_A value of S-2Mn is slightly higher than that obtained for nickel (oxy)hydroxide catalyst by the same procedure (76 kJ mol^{-1}) [80] and for β-NiFeOOH by a different procedure (89 kJ mol^{-1}) [31]. E_A^0 monotonically increases with increasing concentration of all surface hydroxide species (Fig. 8b). Thus, at $\eta = 0$, these species are of hindrance to water adsorption.

Interestingly, at any T_R, the equilibrium kinetics, as monitored by j_0, fastens in the order S-2Ni < S-2Co < S-2Fe < S-2Cr < S-2Mn, i.e., almost in the opposite order as the η-driven kinetics, as monitored by β (Fig. 8c).

The reason for this behavior could be the difference in the oxophilicity of each TM present in S-2X NFs [81–83]. The NFs richer in more oxophilic metals suffer from 'poisoning' of their surface to a larger extent due to the too strong interactions between adsorbed OH and TM cations an consequent stabilization of reaction intermediates.

Finally, for the sake of completeness, the long-term stability of the best performing electrocatalyst (S-2Cr) is evaluated by carrying out chronopotentiometric measurements in 1 M KOH at a current density of 40 mA cm^{-2} for a duration of 14 h (inset of Fig. S19a). The results demonstrate that the catalyst is quite stable: after 14 h of continuous operation, the overpotential increases by ~87 mV. As shown in Fig. S19a, after the application of a current density of 40 mA cm^{-2}, the LSV polarization curve upshifts by ~110 mV in potential, while R_{CT} correspondingly increases by ~43 Ω (Fig. S19b).

4. Conclusion

High-entropy oxides based on five non-equimolar (Cr,Mn,Fe,Co,Ni) combinations are prepared by electrospinning and calcination at 400 °C. The produced nanofibers consist of interconnected ultra-small (<10 nm) crystalline oxide grains, with primary spinel (70–91 wt%) and secondary rock-salt (9–30 wt%) phases and highly defective surface, where O-vacancies (22–34 at.%) and Cr, Co and Ni hydroxides are present.

The HEO NFs are evaluated as electrocatalysts for alkaline water oxidation at 20–60 °C. The results confirm the pivot role played by surface defects, with the surface OV concentration behaving as a reliable descriptor of the process.

At any temperature, in spite of the non-optimal filling of octahedral TM e_g orbitals, the highest activity (lowest η_{10}) pertains to HEO NFs with doubled Cr concentration. The increase in OER temperature from 20 to 60 °C promotes the decrease of charge transfer resistance in all electrocatalysts, resulting in enhanced activity. The electrocatalyst performance at $\eta = 0$, as monitored by the exchange current density, also improves.

Cr hydroxide species on the surface of the catalyst precursors mainly control the activity of the catalyst after activation and the apparent energy barrier E_A for the reaction under applied overpotential (11–33 kJ mol^{-1}). The higher the concentration of surface $Cr(OH)_3$ species on the pre-catalyst, the more active the catalyst is after activation and the lower the E_A.

Differently, all surface hydroxide species cooperate in enhancing the reaction kinetics of activated catalysts (at fixed T_R, β decreases with increasing hydroxide concentration). These species also govern the activation energy barrier E_A^0 at equilibrium (86–147 kJ mol^{-1}). The higher their concentration on the catalyst precursor, the higher the E_A^0.

The slowing down of β at higher T_R is due to 'poisoning' because of other mass transport effects mediated by the stabilization of reaction intermediates on the surface of the fibers richer in more oxophilic metals.

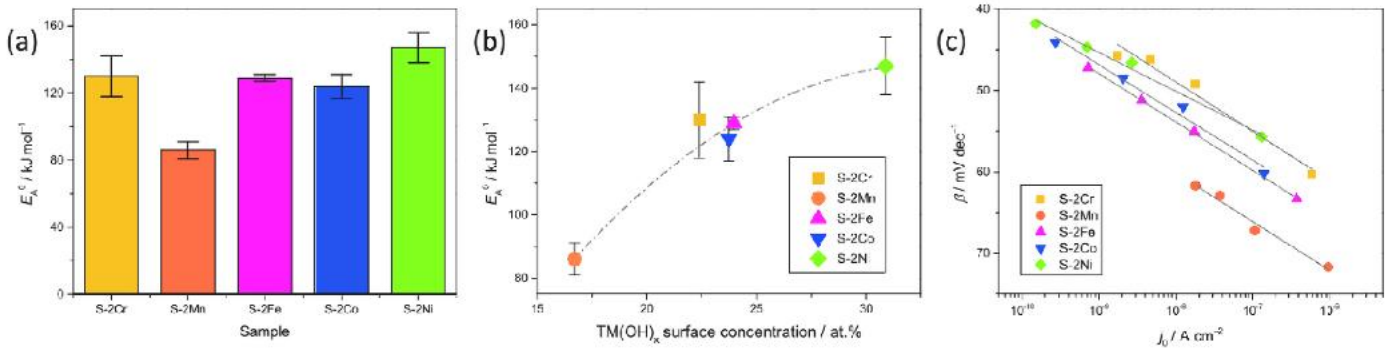

Fig. 8. (a) Activation energy (E_A^0), estimated as the slope of the Arrhenius plots of j_0 and (b) its dependence on the concentration of all surface hydroxide species. (c) Opposite changes of η-driven and equilibrium kinetics (slowdown and fastening, respectively), as monitored by the increase in β and j_0, respectively.

CRediT authorship contribution statement

Claudia Triolo: Validation, Investigation, Formal analysis. **Kaveh Moulaee:** Validation, Investigation, Formal analysis. **Fulvio Bellato:** Formal analysis. **Gioele Pagot:** Investigation, Formal analysis. **Alessandro Ponti:** Writing – review & editing, Supervision, Software, Formal analysis. **Salvatore Maida:** Validation, Investigation, Formal analysis. **Nicola Pinna:** Writing – review & editing, Resources, Investigation. **Giovanni Neri:** Writing – review & editing, Supervision, Resources. **Vito Di Noto:** Writing – review & editing, Supervision, Resources, Investigation, Funding acquisition, Formal analysis, Conceptualization. **Saveria Santangelo:** Writing – review & editing, Writing – original draft, Visualization, Supervision, Resources, Funding acquisition, Formal analysis, Conceptualization.

Declaration of competing interest

The authors declare that they have no known competing financial interests or personal relationships that could have appeared to influence the work reported in this paper.

Acknowledgments

Christoph Erdmann (Humboldt-Universität zu Berlin) is acknowledged for transmission electron microscopy measurements. This research has received funding from: (a) the National Recovery and Resilience Plan (NRRP), Mission 4 Component 2 Investment 1.4 - Call for tender No. 3138 of December 16, 2021 of the Italian Ministry of University and Research, funded by the European Union - NextGenerationEU [Award Number: CNMS named MOST, Concession Decree No. 1033 of June 17, 2022, adopted by the Italian Ministry of University and Research, Spoke 14 "Hydrogen and New Fuels"]; (b) Project "DURALYS - DURAble, Scalable, and Recyclable Components and Cell Designs for Next Generation Alkaline Exchange Membrane Water Electrolysis" funded under the German-Italian Joint call for proposals on "Green Hydrogen Research: A Collaboration to Empower Tomorrow's Energy" within the framework of the collaboration between the German Federal Ministry of Education and Research (BMBF), the Italian Ministry of Foreign Affairs and International Cooperation (MAECI) and the Italian Ministry of University and Research (MUR).

Appendix A. Supplementary data

Supplementary data to this article can be found online at https://doi.org/10.1016/j.jpowsour.2025.237887.

Data availability

Data will be made available on request.

References

[1] J.M.M. Arcos, D.M.F. Santos, The hydrogen color spectrum: techno-economic analysis of the available technologies for hydrogen production, Gases 3 (2023) 25–46, https://doi.org/10.3390/gases3010002.

[2] F. Song, L. Bai, A. Moysiadou, S. Lee, C. Hu, L. Liardet, X. Hu, Transition metal oxides as electrocatalysts for the oxygen evolution reaction in alkaline solutions: an application-inspired Renaissance, J. Am. Chem. Soc. 140 (2018) 7748–7759, https://doi.org/10.1021/jacs.8b04546.

[3] A. Krishnan, R. Ajay, J. Anakha, U.S.K. Namboothiri, Understanding defect chemistry in TMOS involved electrocatalytic OER; an analysis for advancement, Surf. Interfaces 30 (2022) 101942, https://doi.org/10.1016/j.surfin.2022.101942.

[4] X. Yang, S. Liping, L. Qiang, H. Lihua, Z. Hui, Co-prosperity of electrocatalytic activity and stability in high entropy spinel ($Cr_{0.2}$ $Mn_{0.2}$ $Fe_{0.2}$ $Ni_{0.2}$ $Zn_{0.2}$)$_3$ O_4 for the oxygen evolution reaction, J. Mater. Chem. A 10 (2022) 17633–17641, https://doi.org/10.1039/D2TA01376B.

[5] L. He, H. Kang, G. Hou, X. Qiao, X. Jia, W. Qin, X. Wu, Low-temperature synthesis of nano-porous high entropy spinel oxides with high grain boundary density for oxygen evolution reaction, Chem. Eng. J. 460 (2023) 141675, https://doi.org/10.1016/j.cej.2023.141675.

[6] L. Xiao, Z. Wang, J. Guan, Optimization strategies of high-entropy alloys for electrocatalytic applications, Chem. Sci. 14 (2023) 12850–12868, https://doi.org/10.1039/D3SC04962K.

[7] C. Triolo, S. Schweidler, L. Lin, G. Pagot, V. Di Noto, B. Breitung, S. Santangelo, Evaluation of electrospun spinel-type high-entropy ($Cr_{0.2}$ $Mn_{0.2}$ $Fe_{0.2}$ $Co_{0.2}$ $Ni_{0.2}$)$_3$ O_4 , ($Cr_{0.2}$ $Mn_{0.2}$ $Fe_{0.2}$ $Co_{0.2}$ $Zn_{0.2}$)$_3$ O_4 and ($Cr_{0.2}$ $Mn_{0.2}$ $Fe_{0.2}$ $Ni_{0.2}$ $Zn_{0.2}$)$_3$ O_4 oxide nanofibers as electrocatalysts for oxygen evolution in alkaline medium, Energy Adv 2 (2023) 667–678, https://doi.org/10.1039/D3YA00062A.

[8] C.-H. Su, C.-W. Kung, T.-H. Chang, H.-C. Lu, K.-C. Ho, Y.-C. Liao, Inkjet-printed porphyrinic metal organic framework thin films for electrocatalysis, J. Mater. Chem. A 4 (2016) 11094–11102, https://doi.org/10.1039/C6TA03547G.

[9] J. Han, J. Sun, S. Chen, S. Zhang, L. Qi, A. Husile, J. Guan, Structure Activity relationships in oxygen electrocatalysis, Adv. Mater. 36 (2024) 2408139, https://doi.org/10.1002/adma.202408139.

[10] M. Chen, J. Guan, Achievements and challenges in cobalt-based catalysts for water electrolysis, Chem. Eng. J. 500 (2024) 157080, https://doi.org/10.1016/j.cej.2024.157080.

[11] C. Triolo, K. Moulaee, A. Ponti, G. Pagot, V. Di Noto, N. Pinna, G. Neri, S. Santangelo, Spinel-Structured high-entropy oxide nanofibers as electrocatalysts for oxygen evolution in alkaline solution: effect of metal combination and calcination temperature, Adv. Funct. Mater. 34 (2024) 2306375, https://doi.org/10.1002/adfm.202306375.

[12] F. Calle-Vallejo, N.G. Inoglu, H.-Y. Su, J.I. Martínez, I.C. Man, M.T.M. Koper, J. R. Kitchin, J. Rossmeisl, Number of outer electrons as descriptor for adsorption processes on transition metals and their oxides, Chem. Sci. 4 (2013) 1245, https://doi.org/10.1039/c2sc21601a.

[13] C. Wei, Z. Feng, G.G. Scherer, J. Barber, Y. Shao-Horn, Z.J. Xu, Cations in octahedral sites: a descriptor for oxygen electrocatalysis on transition-metal spinels, Adv. Mater. 29 (2017) 1606800, https://doi.org/10.1002/adma.201606800.

[14] K. Vezzù, C. Triolo, K. Moulaee, G. Pagot, A. Ponti, N. Pinna, G. Neri, S. Santangelo, V. Di Noto, Interplay between calcination temperature and alkaline oxygen evolution of Electrospun High-Entropy ($Cr_{1/5}$ $Mn_{1/5}$ $Fe_{1/5}$ $Co_{1/5}$ $Ni_{1/5}$)$_3$ O_4 nanofibers, Small 21 (2025) 2408319, https://doi.org/10.1002/smll.202408319.

[15] T.X. Nguyen, Y. Liao, C. Lin, Y. Su, J. Ting, Advanced high Entropy Perovskite oxide electrocatalyst for oxygen evolution reaction, Adv. Funct. Mater. 31 (2021) 2101632, https://doi.org/10.1002/adfm.202101632.

[16] S. Sun, Y. Sun, Y. Zhou, S. Xi, X. Ren, B. Huang, H. Liao, L.P. Wang, Y. Du, Z.J. Xu, Shifting oxygen charge towards octahedral metal: a way to promote water oxidation on cobalt spinel oxides, Angew. Chem. 131 (2019) 6103–6108, https://doi.org/10.1002/ange.201902114.

[17] M. Li, M. Song, W. Ni, Z. Xiao, Y. Li, J. Jia, S. Wang, Y. Wang, Activating surface atoms of high entropy oxides for enhancing oxygen evolution reaction, Chin. Chem. Lett. 34 (2023) 107571, https://doi.org/10.1016/j.cclet.2022.05.085.

[18] J. Bao, X. Zhang, B. Fan, J. Zhang, M. Zhou, W. Yang, X. Hu, H. Wang, B. Pan, Y. Xie, Ultrathin spinel-structured nanosheets rich in oxygen deficiencies for enhanced electrocatalytic water oxidation, Angew. Chem. 127 (2015) 7507–7512, https://doi.org/10.1002/ange.201502226.

[19] T. Liu, Z. Feng, Q. Li, J. Yang, C. Li, M. Dupuis, Role of oxygen vacancies on oxygen evolution reaction activity: β-Ga_2 O_3 as a case Study, Chem. Mater. 30 (2018) 7714–7726, https://doi.org/10.1021/acs.chemmater.8b03015.

[20] K. Zhu, F. Shi, X. Zhu, W. Yang, The roles of oxygen vacancies in electrocatalytic oxygen evolution reaction, Nano Energy 73 (2020) 104761, https://doi.org/10.1016/j.nanoen.2020.104761.

[21] A. Badreldin, A.E. Abusrafa, A. Abdel-Wahab, Oxygen-deficient perovskites for oxygen evolution reaction in alkaline media: a review, Emergent Mater 3 (2020) 567–590, https://doi.org/10.1007/s42247-020-00123-z.

[22] E. Marelli, J. Gazquez, E. Poghosyan, E. Müller, D.J. Gawryluk, E. Pomjakushina, D. Sheptyakov, C. Piamonteze, D. Aegerter, T.J. Schmidt, M. Medarde, E. Fabbri, Correlation between oxygen vacancies and oxygen evolution reaction activity for a model electrode: $PrBaCo_2$ $O_{5-\delta}$, Angew. Chem. Int. Ed. 60 (2021) 14609–14619, https://doi.org/10.1002/anie.202103151.

[23] S. Roy, N. Devaraj, K. Tarafder, C. Chakraborty, S. Roy, The role of synthesis *vis-à-vis* the oxygen vacancies of Co_3 O_4 in the oxygen evolution reaction, New J. Chem. 46 (2022) 6539–6548, https://doi.org/10.1039/D2NJ00219A.

[24] J. Baek, M.D. Hossain, P. Mukherjee, J. Lee, K.T. Winther, J. Leem, Y. Jiang, W. C. Chueh, M. Bajdich, X. Zheng, Synergistic effects of mixing and strain in high entropy spinel oxides for oxygen evolution reaction, Nat. Commun. 14 (2023) 5936, https://doi.org/10.1038/s41467-023-41359-7.

[25] X. Liu, K. Ni, B. Wen, R. Guo, C. Niu, J. Meng, Q. Li, P. Wu, Y. Zhu, X. Wu, L. Mai, Deep reconstruction of nickel-based precatalysts for water oxidation catalysis, ACS Energy Lett. 4 (2019) 2585–2592, https://doi.org/10.1021/acsenergylett.9b01922.

[26] T. Guo, L. Li, Z. Wang, Recent development and future perspectives of amorphous transition metal-based electrocatalysts for oxygen evolution reaction, Adv. Energy Mater. 12 (2022) 2200827, https://doi.org/10.1002/aenm.202200827.

[27] L. Fan, B. Zhang, B.J.J. Timmer, N.V.R.A. Dharanipragada, X. Sheng, C.-W. Tai, F. Zhang, T. Liu, Q. Meng, A.K. Inge, L. Sun, Promoting the Fe(VI) active species generation by structural and electronic modulation of efficient iron oxide based water oxidation catalyst without Ni or Co, Nano Energy 72 (2020) 104656, https://doi.org/10.1016/j.nanoen.2020.104656.

[28] C.R. Davidson, S. Srinivasan, Influence of nickel oxide transformation reaction on oxygen evolution kinetics as ascertained by temperature effects, J. Electrochem. Soc. 127 (1980) 1060–1063, https://doi.org/10.1149/1.2129817.

[29] C. Davidson, G. Kissel, S. Srinivasan, Electrode kinetics of the oxygen evolution reaction at NiCo2O4 from 30% KOH, J. Electroanal. Chem. Interfacial

Electrochem. 132 (1982) 129–135, https://doi.org/10.1016/0022-0728(82)85012-2.
[30] G. Zhang, H. Wang, J. Yang, Q. Zhao, L. Yang, H. Tang, C. Liu, H. Chen, Y. Lin, F. Pan, Temperature effect on Co-Based catalysts in oxygen evolution reaction, Inorg. Chem. 57 (2018) 2766–2772, https://doi.org/10.1021/acs.inorgchem.7b03168.
[31] Z. Lin, P. Bu, Y. Xiao, Q. Gao, P. Diao, β- and γ-NiFeOOH electrocatalysts for an efficient oxygen evolution reaction: an electrochemical activation energy aspect, J. Mater. Chem. A 10 (2022) 20847–20855, https://doi.org/10.1039/D2TA04688A.
[32] T.A. Zegeye, W.-T. Chen, C.-C. Hsu, J.A.A. Valinton, C.-H. Chen, Activation energy assessing potential-dependent activities and site reconstruction for oxygen evolution, ACS Energy Lett. 7 (2022) 2236–2243, https://doi.org/10.1021/acsenergylett.2c01103.
[33] G. Shi, T. Tano, D.A. Tryk, M. Yamaguchi, A. Iiyama, M. Uchida, K. Iida, C. Arata, S. Watanabe, K. Kakinuma, Temperature dependence of oxygen evolution reaction activity in alkaline solution at Ni–Co oxide catalysts with Amorphous/Crystalline surfaces, ACS Catal. 12 (2022) 14209–14219, https://doi.org/10.1021/acscatal.2c02586.
[34] Z. Lin, Q. Gao, P. Diao, Promoting the electrocatalytic oxygen evolution reaction on NiCo2O4 with infrared-thermal effect: a strategy to utilize the infrared solar energy to reduce activation energy during water splitting, J. Colloid Interface Sci. 638 (2023) 54–62, https://doi.org/10.1016/j.jcis.2023.01.130.
[35] F. Pantò, Z. Dahrouch, A. Saha, S. Patanè, S. Santangelo, C. Triolo, Photocatalytic degradation of methylene blue dye by porous zinc oxide nanofibers prepared via electrospinning: when defects become merits, Appl. Surf. Sci. 557 (2021) 149830, https://doi.org/10.1016/j.apsusc.2021.149830.
[36] A. Patriarchi, C. Triolo, L. Minnetti, M.Á. Muñoz-Márquez, F. Nobili, S. Santangelo, Evaluation of high-entropy (Cr, Mn, Fe, Co, ni)-oxide nanofibers and nanoparticles as passive fillers for solid composite electrolytes, Electrochim. Acta 512 (2025) 145425, https://doi.org/10.1016/j.electacta.2024.145425.
[37] S.S. Aamlid, M. Oudah, J. Rottler, A.M. Hallas, Understanding the role of entropy in high entropy oxides, J. Am. Chem. Soc. 145 (2023) 5991–6006, https://doi.org/10.1021/jacs.2c11608.
[38] M.J. Hytch, Analysis of variations in structure from high resolution electron microscope images by combining real space and fourier space information, Microsc. Microanal. Microstruct. 8 (1997) 41–57, https://doi.org/10.1051/mmm:1997105.
[39] J.L. Rouvière, E. Sarigiannidou, Theoretical discussions on the geometrical phase analysis, Ultramicroscopy 106 (2005) 1–17, https://doi.org/10.1016/j.ultramic.2005.06.001.
[40] J.E. Castle, in: D. Briggs, M.P. Seah (Eds.), Practical Surface Analysis by Auger and X-Ray Photoelectron Spectroscopy, vol. 6, John Wiley and Sons Ltd, Chichester, 1983, p. 533, https://doi.org/10.1002/sia.740060611 (1984) 302–302 44.50, Surface & Interface Analysis.
[41] D.A. Shirley, High-Resolution X-Ray photoemission spectrum of the valence bands of gold, Phys. Rev. B 5 (1972) 4709–4714, https://doi.org/10.1103/PhysRevB.5.4709.
[42] Y. Zhang, W. Dai, P. Zhang, T. Lu, Y. Pan, In-situ electrochemical tuning of (CoNiMnZnFe)3O3.2 high-entropy oxide for efficient oxygen evolution reactions, J. Alloys Compd. 868 (2021) 159064, https://doi.org/10.1016/j.jallcom.2021.159064.
[43] M. Einert, M. Wellin, N. Bahadorani, C. Dietz, S. Lauterbach, J.P. Hofmann, Mesoporous high entropy oxide thin films: electrocatalytic water oxidation on high-surface-area spinel $(Cr_{0.2}Mn_{0.2}Fe_{0.2}Co_{0.2}Ni_{0.2})_3O_4$ electrodes, ACS Appl. Energy Mater. 5 (2022) 717–730, https://doi.org/10.1021/acsaem.1c03190.
[44] A. Senthamizhan, B. Balusamy, Z. Aytac, T. Uyar, Grain boundary engineering in electrospun ZnO nanostructures as promising photocatalysts, CrystEngComm 18 (2016) 6341–6351, https://doi.org/10.1039/C6CE00693K.
[45] D. Hu, R. Wang, P. Du, G. Li, Y. Wang, D. Fan, X. Pan, Electrospinning Ru doped Co3O4 porous nanofibers as promising bifunctional catalysts for oxygen evolution and oxygen reduction reactions, Ceram. Int. 48 (2022) 6549–6555, https://doi.org/10.1016/j.ceramint.2021.11.202.
[46] A. Ponti, C. Triolo, B. Petrovičovà, A.M. Ferretti, G. Pagot, W. Xu, V. Di Noto, N. Pinna, S. Santangelo, Structure and magnetism of electrospun porous high-entropy $(Cr_{1/5}Mn_{1/5}Fe_{1/5}Co_{1/5}Ni_{1/5})_3O_4$, $(Cr_{1/5}Mn_{1/5}Fe_{1/5}Co_{1/5}Zn_{1/5})_3O_4$ and $(Cr_{1/5}Mn_{1/5}Fe_{1/5}Ni_{1/5}Zn_{1/5})_3O_4$ spinel oxide nanofibers, Phys. Chem. Chem. Phys. 25 (2023) 2212–2226, https://doi.org/10.1039/D2CP05142G.
[47] C. Triolo, W. Xu, B. Petrovičovà, N. Pinna, S. Santangelo, Evaluation of entropy-stabilized $(Mg_{0.2}Co_{0.2}Ni_{0.2}Cu_{0.2}Zn_{0.2})O$ oxides produced via solvothermal method or electrospinning as anodes in lithium-ion batteries, Adv. Funct. Mater. 32 (2022) 2202892, https://doi.org/10.1002/adfm.202202892.
[48] R.S. Yadav, I. Kuřitka, J. Vilcakova, J. Havlica, J. Masilko, L. Kalina, J. Tkacz, J. Švec, V. Enev, M. Hajdúchová, Impact of grain size and structural changes on magnetic, dielectric, electrical, impedance and modulus spectroscopic characteristics of $CoFe_2O_4$ nanoparticles synthesized by honey mediated sol-gel combustion method, Adv. Nat. Sci. Nanosci. Nanotechnol. 8 (2017) 045002, https://doi.org/10.1088/2043-6254/aa853a.
[49] V. D'Ippolito, G.B. Andreozzi, D. Bersani, P.P. Lottici, Raman fingerprint of chromate, aluminate and ferrite spinels, J. Raman Spectrosc. 46 (2015) 1255–1264, https://doi.org/10.1002/jrs.4764.
[50] C. Triolo, M. Maisuradze, M. Li, Y. Liu, A. Ponti, G. Pagot, V. Di Noto, G. Aquilanti, N. Pinna, M. Giorgetti, S. Santangelo, Charge storage mechanism in electrospun spinel-structured High-Entropy $(Mn_{0.2}Fe_{0.2}Co_{0.2}Ni_{0.2}Zn_{0.2})_3O_4$ oxide nanofibers as anode material for li-ion batteries, Small 19 (2023) 2304585, https://doi.org/10.1002/smll.202304585.
[51] V.I. Nefedov, YaV. Salyn, G. Leonhardt, R. Scheibe, A comparison of different spectrometers and charge corrections used in X-ray photoelectron spectroscopy, J. Electron. Spectrosc. Relat. Phenom. 10 (1977) 121–124, https://doi.org/10.1016/0368-2048(77)85010-X.
[52] G. Mattogno, C. Ferragina, M.A. Massucci, P. Patrono, A. La Ginestra, X-ray photoelectron spectroscopic evidence of interlayer complex formation between Co (II) and N-heterocycles in α-Zr(hpo4)2 · H2O, J. Electron. Spectrosc. Relat. Phenom. 46 (1988) 285–295, https://doi.org/10.1016/0368-2048(88)85026-6.
[53] T.J. Chuang, C.R. Brundle, D.W. Rice, Interpretation of the x-ray photoemission spectra of cobalt oxides and cobalt oxide surfaces, Surf. Sci. 59 (1976) 413–429, https://doi.org/10.1016/0039-6028(76)90026-1.
[54] K.S. Kim, N. Winograd, X-ray photoelectron spectroscopic studies of nickel-oxygen surfaces using oxygen and argon ion-bombardment, Surf. Sci. 43 (1974) 625–643, https://doi.org/10.1016/0039-6028(74)90281-7.
[55] C.P. Li, A. Proctor, D.M. Hercules, Curve fitting analysis of ESCA Ni 2p Spectra of nickel-oxygen compounds and Ni/Al_2O_3 catalysts, Appl. Spectrosc. 38 (1984) 880–886, https://doi.org/10.1366/0003702844554530.
[56] F. Desimoni, C. Malitesta, P.G. Zambonin, J.C. Rivière, An x-ray photoelectron spectroscopic study of some chromium–oxygen systems, Surf. Interface Anal. 13 (1988) 173–179, https://doi.org/10.1002/sia.740130210.
[57] B. Wichterlová, L. Krajčíková, Z. Tvarůžková, S. Beran, Chromium ions in zeolites. Part 4.—X-ray photoelectron spectroscopic study of chromium valence states in the surface layers of CrY zeolites, J. Chem. Soc., Faraday Trans. 1 80 (1984) 2639, https://doi.org/10.1039/f19848002639.
[58] J.P. Bonnelle, J. Grimblot, A. D'huysser, Influence de la polarisation des liaisons sur les spectres esca des oxydes de cobalt, J. Electron. Spectrosc. Relat. Phenom. 7 (1975) 151–162, https://doi.org/10.1016/0368-2048(75)80047-8.
[59] G. Pagot, M.C. Cassani, F. Gambassi, B. Ballarin, D. Nanni, M. Coi, D. Barreca, E. Boanini, V. Di Noto, Propargyl carbamate-functionalized Cu(II)-metal organic framework after reaction with chloroauric acid: an x-ray photoelectron spectroscopy data record, Surf. Sci. Spectra 29 (2022) 024007, https://doi.org/10.1116/6.0001950.
[60] B. Strohmeier, Surface spectroscopic characterization of the interaction between zinc ions and $gamma;-alumina, J. Catal. 86 (1984) 266–279, https://doi.org/10.1016/0021-9517(84)90372-5.
[61] T.J. Frankcombe, Y. Liu, Interpretation of oxygen 1s X-ray Photoelectron spectroscopy of ZnO, Chem. Mater. 35 (2023) 5468–5474, https://doi.org/10.1021/acs.chemmater.3c00801.
[62] J. Haber, J. Stoch, L. Ungier, X ray photoelectron spectra of oxygen in oxides of Co, Ni, Fe and Zn, J. Electron. Spectrosc. Relat. Phenom. 9 (1976) 459–467, https://doi.org/10.1016/0368-2048(76)80064-3.
[63] B.J. Tan, K.J. Klabunde, P.M.A. Sherwood, XPS studies of solvated metal atom dispersed (SMAD) catalysts. Evidence for layered cobalt-manganese particles on alumina and silica, J. Am. Chem. Soc. 113 (1991) 855–861, https://doi.org/10.1021/ja00003a019.
[64] V. Maruthapandian, M. Mathankumar, V. Saraswathy, B. Subramanian, S. Muralidharan, Study of the oxygen evolution reaction catalytic behavior of Co *x Ni 1– x Fe2 O4 in alkaline medium*, ACS Appl. Mater. Interfaces 9 (2017) 13132–13141, https://doi.org/10.1021/acsami.6b16685.
[65] S. Sun, Y. Sun, Y. Zhou, J. Shen, D. Mandler, R. Neumann, Z.J. Xu, Switch of the rate-determining step of water oxidation by spin-selected electron transfer in spinel oxides, Chem. Mater. 31 (2019) 8106–8111, https://doi.org/10.1021/acs.chemmater.9b02737.
[66] X. Chen, Z. Zhang, Y. Chen, R. Xu, C. Song, T. Yuan, W. Tang, X. Gao, N. Wang, L. Cui, Research advances in earth-abundant-element-based electrocatalysts for oxygen evolution reaction and oxygen reduction reaction, Energy Mater (2023), https://doi.org/10.20517/energymater.2023.12.
[67] J. Sun, N. Guo, Z. Shao, K. Huang, Y. Li, F. He, Q. Wang, A Facile strategy to construct amorphous spinel-based electrocatalysts with massive oxygen vacancies using ionic liquid dopant, Adv. Energy Mater. 8 (2018) 1800980, https://doi.org/10.1002/aenm.201800980.
[68] S. Wahl, S.M. El-Refaei, A.G. Buzanich, P. Amsalem, K. Lee, N. Koch, M. Doublet, N. Pinna, Zn0.35 Co0.65 O – a stable and highly active oxygen evolution catalyst formed by zinc leaching and tetrahedral coordinated cobalt in Wurtzite structure, Adv. Energy Mater. 9 (2019) 1900328, https://doi.org/10.1002/aenm.201900328.
[69] S.P. Babu, A. Palch, Recent developments on cr-based electrocatalysts for the oxygen evolution reaction in alkaline media, ChemCatChem 14 (2022) e202200364, https://doi.org/10.1002/cctc.202200364.
[70] W. Liu, J. Bao, L. Xu, M. Guan, Y. Lei, Chromium-modulated multifunctional electrocatalytic activities of spinel oxide for Zn-air batteries and overall water splitting, J. Power Sources 479 (2020) 229099, https://doi.org/10.1016/j.jpowsour.2020.229099.
[71] J. Yan, L. Kong, Y. Ji, J. White, Y. Li, J. Zhang, P. An, S. Liu, S.-T. Lee, T. Ma, Single atom tungsten doped ultrathin α-Ni(OH)2 for enhanced electrocatalytic water oxidation, Nat. Commun. 10 (2019) 2149, https://doi.org/10.1038/s41467-019-09845-z.
[72] Y. Wang, S. Liu, Y. Qin, Y. Zhao, L. Liu, D. Zhang, J. Liu, Y. Liu, A. Chu, H. Wu, B. Jia, X. Qu, H. Li, M. Qin, Chromium promotes phase transformation to active oxyhydroxide for efficient oxygen evolution, ACS Catal. 14 (2024) 13759–13767, https://doi.org/10.1021/acscatal.4c03974.
[73] Z. Kou, X. Li, L. Zhang, W. Zang, X. Gao, J. Wang, Dynamic surface chemistry of catalysts in oxygen evolution reaction, Small Science 1 (2021) 2100011, https://doi.org/10.1002/smsc.202100011.
[74] B. Talluri, K. Yoo, J. Kim, High entropy spinel metal oxide (CoCrFeMnNi)3O4 nanoparticles as novel efficient electrocatalyst for methanol oxidation and oxygen

evolution reactions, J. Environ. Chem. Eng. 10 (2022) 106932, https://doi.org/10.1016/j.jece.2021.106932.
[75] M. Harada, F. Kotegawa, M. Kuwa, Structural changes of spinel MCo2 O4 (M = Mn, Fe, Co, Ni, and zn) electrocatalysts during the oxygen evolution reaction investigated by in situ X-ray absorption spectroscopy, ACS Appl. Energy Mater. 5 (2022) 278–294, https://doi.org/10.1021/acsaem.1c02824.
[76] L. Gao, X. Cui, C.D. Sewell, J. Li, Z. Lin, Recent advances in activating surface reconstruction for the high-efficiency oxygen evolution reaction, Chem. Soc. Rev. 50 (2021) 8428–8469, https://doi.org/10.1039/D0CS00962H.
[77] Y. Zhang, W. Dai, P. Zhang, T. Lu, Y. Pan, In-situ electrochemical tuning of (CoNiMnZnFe)3O3.2 high-entropy oxide for efficient oxygen evolution reactions, J. Alloys Compd. 868 (2021) 159064, https://doi.org/10.1016/j.jallcom.2021.159064.
[78] L. Fan, B. Zhang, B.J.J. Timmer, N.V.R.A. Dharanipragada, X. Sheng, C.-W. Tai, F. Zhang, T. Liu, Q. Meng, A.K. Inge, L. Sun, Promoting the Fe(VI) active species generation by structural and electronic modulation of efficient iron oxide based water oxidation catalyst without Ni or Co, Nano Energy 72 (2020) 104656, https://doi.org/10.1016/j.nanoen.2020.104656.
[79] V.D. Noto, G. Pagot, K. Vezzù, E. Negro, P. Sgarbossa, Electrochemical fundamentals, in: N. Alonso-Vante, V. Di Noto (Eds.), Electrocatalysis for Membrane Fuel Cells, first ed., Wiley, 2023, pp. 69–109, https://doi.org/10.1002/9783527830572.ch3.
[80] J.R. Swierk, S. Klaus, L. Trotochaud, A.T. Bell, T.D. Tilley, Electrochemical study of the energetics of the oxygen evolution reaction at nickel iron (oxy)Hydroxide catalysts, J. Phys. Chem. C 119 (2015) 19022–19029, https://doi.org/10.1021/acs.jpcc.5b05861.
[81] R. Subbaraman, D. Tripkovic, K.-C. Chang, D. Strmcnik, A.P. Paulikas, P. Hirunsit, M. Chan, J. Greeley, V. Stamenkovic, N.M. Markovic, Trends in activity for the water electrolyser reactions on 3d M(Ni,Co,Fe,Mn) hydr(oxy)oxide catalysts, Nat. Mater. 11 (2012) 550–557, https://doi.org/10.1038/nmat3313.
[82] K.P. Kepp, A quantitative scale of oxophilicity and thiophilicity, Inorg. Chem. 55 (2016) 9461–9470, https://doi.org/10.1021/acs.inorgchem.6b01702.
[83] G.O. Kayode, M.M. Montemore, Factors controlling oxophilicity and carbophilicity of transition metals and main group metals, J. Mater. Chem. A 9 (2021) 22325–22333, https://doi.org/10.1039/D1TA06453C.